🔓 OPEN ACCESS

Observation of the most H₂-dense filled ice under high pressure

Umbertoluca Ranieri[a,b,1] (ID), Simone Di Cataldo[a,c,1] (ID), Maria Rescigno[a,d], Lorenzo Monacelli[e], Richard Gaal[d] (ID), Mario Santoro[f,g] (ID), Leon Andriambariarijaona[h], Paraskevas Parisiades[h] (ID), Cristiano De Michele[a] (ID), and Livia Eleonora Bove[a,d,h,2] (ID)

Hydrogen hydrates are among the basic constituents of our solar system's outer planets, some of their moons, as well Neptune-like exo-planets. The details of their high-pressure phases and their thermodynamic conditions of formation and stability are fundamental information for establishing the presence of hydrogen hydrates in the interior of those celestial bodies, for example, against the presence of the pure components (water ice and molecular hydrogen). Here, we report a synthesis path and experimental observation, by X-ray diffraction and Raman spectroscopy measurements, of the most H₂-dense phase of hydrogen hydrate so far reported, namely the compound 3 (or C₃). The detailed characterisation of this hydrogen-filled ice, based on the crystal structure of cubic ice I (ice Ic), is performed by comparing the experimental observations with first-principles calculations based on density functional theory and the stochastic self-consistent harmonic approximation. We observe that the extreme (up to 90 GPa and likely beyond) pressure stability of this hydrate phase is due to the close-packed geometry of the hydrogen molecules caged in the ice Ic skeleton.

clathrate hydrates | phase transitions | high pressure | Raman | ab initio simulations

Gas hydrates are probably more abundant than rocky materials or all polymorphs of pure ice in giant icy and gaseous planets like Jupiter, Saturn, Uranus, and Neptune, as well as in Neptune-like exo-planets, and hydrogen hydrate must account for a significant part of them. These planets have a H_2 and He gases–dominated atmosphere and an interior mostly constituted by planetary ices (H_2O, CH_4, and NH_3) subjected to high pressure and temperature. Molecular hydrogen potentially contributes significantly to the volatile budget of other water-rich objects of various sizes, as witnessed by the detection of H_2 in the vapour plume of Saturn's tiny moon Enceladus, in abundances comparable to NH_3 and CO_2 (1) or in other trans-Neptunian objects (2, 3). The presence of H_2 in significant amount may have a major impact on the planetary habitability, by affecting both atmospheric thermal budget and interior redox state, particularly in water-rich worlds (4). Depending on the size of the planet or moon, H_2 may be incorporated in the planetary interior in different (solid) hydrate phases binding the gas at fairly high temperatures. The crystalline structure formed and the fraction of hydrogen stored in these systems depend on the specific thermodynamic conditions.

Laboratory experiments have indeed discovered that mixtures of water (or ice) and hydrogen gas spontaneously crystallize into a hydrogen clathrate hydrate under moderate pressures (above 0.1 GPa at temperatures below 270 K) (5). This non-stoichiometric guest–host compound is characterized by polyhedral cavities constituted of hydrogen-bonded water molecules encaging a variable amount of H_2 molecules in the well-known clathrate structure II (or sII), which is also observed for the hydrates of other gas species (6). Such a phase provides a higher stability for H_2 when compared to its pure phase sublimation equilibrium. As for some other gas hydrates, at higher pressures, the so-called "filled ice" structures form, in which the water host sublattice is no longer formed by cages but resembles one of the crystalline phases of pure water ice (7, 8). Upon compression, hydrogen hydrate goes through a sequence of phase transitions into a variety of crystalline phases with generally an increasing fraction of H_2 molecules per H_2O. In addition to sII, the phases C_{-1} (9), C_0 (10–12), C_1 (13), C_1' (14), and C_2 (13) have been reported over the pressure range up to ~3 GPa. Yet, this variety is small compared to the structural diversity exhibited by the many water ice phases (15, 16), and it is likely that new hydrogen hydrate compounds remain to be discovered. In phase C_2, the water sublattice forms the cubic ice Ic structure and the H_2 to H_2O molar ratio is of 1. Another phase, called C_3, which should share its water sublattice with C_2 and should have an extremely high H_2 to H_2O molar ratio of 2, was calculated to become stable above 38 GPa (17) but no experimental observation of this new hydrate exists so far. While several computational (18–22) studies of hydrogen hydrates at high pressure have been previously reported, the only experimental datasets existing above 3 GPa in the literature essentially come

Significance

Clathrate hydrates of methane and other alkanes are a natural part of the deep-sea and permafrost environments and important gas reservoirs. Still other gas hydrate phases, not (yet) known in nature, have been characterized in the laboratory. Here, combination of high pressures and high temperatures was used to synthesize a hydrogen hydrate phase which has the structure of cubic ice for the water framework and twice as many H_2 as H_2O molecules in the unit cell, namely the highest gas-to-water molar ratio reported to date in any crystalline solid made of water and gas. This water–hydrogen compound is most likely stable up to pressures beyond the limit of the current experiments and might be abundant inside extra-terrestrial objects.

[1]U.R. and S.D.C. contributed equally to this work.

[2]To whom correspondence may be addressed. Email: livia.bove@epfl.ch.

from a single group (23–25). The authors showed the stability of hydrogen hydrate upon compression to 70 GPa by Raman spectroscopy and reported the observation of a small tetragonal distortion of the high-pressure C_2 phase above 20 GPa by X-ray diffraction (XRD), followed by a structural transition to an unsolved phase at about 45 GPa (which is not the predicted C_3 phase) (24). Another study reported no structural transition at 45 GPa but pressure-induced amorphization at 65 GPa for the $D_2O–H_2$ system (not for $H_2O–H_2$) (25).

The existence of the elusive C_3 phase thus remains to be proven, and the consequences of it on the volatile balance of large icy and gas planets' atmospheres and on the modelling of their interior to be investigated. Furthermore, the C_3 phase would be the most gas-rich hydrate ever discovered, with a hydrogen volume density higher than 0.25 kg/L, i.e., four times that of liquid H_2, stored in a non-reactive, environmentally favorable water frame. Unveiling the conditions of formation of this remarkable hydrogen-dense hydrate, understanding the way water and hydrogen can fit in such a tight volume minimizing their repulsive interaction, and probing the possibility to recover such a structure at ambient pressure would pave the way to new opportunities of storage of hydrogen at high concentrations in hydrates. Hydrates constitute indeed a technologically attractive hosting environment for physical H_2 storage due to their appealing properties such as low energy consumption for charge and discharge, safety, cost-effectiveness, and environmentally friendly nature (26). The identification of a hydrogen hydrate phase trapping hydrogen at mass fractions surpassing those of the best materials presently used for hydrogen storage would boost the research for devising ways to increase H_2 storage capacity at more realistic engineering pressures.

In this work, we investigate the room-temperature and high-pressure binary phase diagram of water and hydrogen by coupling synchrotron XRD and Raman spectroscopy measurements in a diamond anvil cell (DAC) up to 90 GPa. In some experimental runs, laser heating (LH) of the sample was employed at 40 GPa to overcome possible kinetic barriers preventing the transition to the thermodynamic ground state. First-principles calculations based on evolutionary algorithms for crystal structure prediction (27, 28), density functional theory (DFT), and the stochastic self-consistent harmonic approximation (SSCHA) (29, 30) were employed to accurately simulate the structural, thermodynamical, dynamical, and optical properties of the studied phases. Our results demonstrate the existence of the predicted (17) hydrogen-dense C_3 phase, giving a rationale for its synthesis, as well as an explanation of the lack of its observation in previous experiments. The paper is structured as follows: First, we will present the computational and experimental results (from XRD and then Raman spectroscopy), and then, we will discuss the peculiar structural features of the C_3 phase that enable its stability up to Megabar pressures.

Results

We computed the phase diagram of hydrogen and water using ab initio crystal structure prediction based on density functional theory at 20, 40, and 200 GPa and computed the equation of state of stable phases at a large number of intermediate pressures (see *SI Appendix* for further details and *SI Appendix*, Figs. S1–S6 therein). Fig. 1 shows a summary of the pressure stability of the different hydrogen hydrate phases. Computationally, we find the C_2 phase to be stable up to about 20 GPa, while the C_3 phase becomes stable only above 30 GPa (see the calculated enthalpy in *SI Appendix*, Fig. S4) leaving a region of about 10 GPa in

which no hydrate phase is stable. However, as we will discuss more in-depth below, the C_2 phase can experimentally remain metastable up to higher pressures, and only when sufficiently heated, it transforms into the C_3 phase, which is then observed up to the highest investigated pressure of this work (90 GPa). On the other hand, the samples that were compressed without laser heating remained in the C_2 phase, which is metastable up to the highest investigated pressure (Fig. 1).

More than ten different Raman experiments have been performed on as many sample loadings and three of them have been coupled to synchrotron XRD measurements. In three of the experimental runs, laser heating was employed, heating the sample to 1,200(200) K at about 40 GPa, followed by rapid cooling (quenching) due to the high thermal conductivity of diamond. The high-pressure cells had been loaded at liquid nitrogen temperature with hydrogen hydrate samples in the clathrate phase sII, which formed the C_2 phase and excess water ice (because of the difference in composition between the sII and C_2 hydrogen hydrates) upon compression to pressures above 2–3 GPa, as expected from the extensive previous literature. Upon further compression to about 20 GPa and above, we start observing progressive appearance of pure solid H_2 in the sample (clearly identified by its Raman vibron signal), highly likely because of partial decomposition of hydrogen hydrate into its components, which is consistent with the region of instability in Fig. 1. For further details on the sample preparation and experimental setups, as well as computational details, we refer the reader to see *Materials and Methods*.

XRD Measurements and Related Computational Results. In Fig. 2, we report examples of XRD 2D images and patterns,
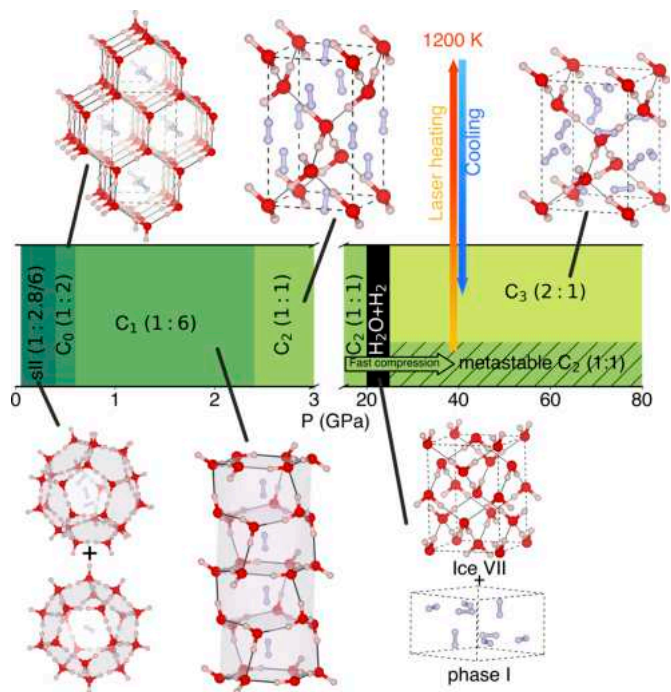

Fig. 1. Calculated structural transition sequence of hydrogen hydrate as a function of pressure, with regions of thermodynamical stability of different phases indicated by different colors. $H_2:H_2O$ molar ratios are reported in parenthesis. "H_2O+H_2" indicates that no hydrate phase is thermodynamically stable in the corresponding pressure range. Ball-and-stick models of the crystal structures are also reported (O atoms in red, H atoms in white, and H_2 molecules in cyan). Experimentally, phase C_2 can be compressed to pressures above its range of stability as a metastable phase. Upon laser heating at about 40 GPa, it transforms into phase C_3.

before and after laser heating of the sample, as well as the obtained pressure–volume equations of state for the phases C_2 and C_3, which we also compare to the results of our numerical simulations. The C_2 and C_3 phases, which feature proton-disordered H_2O molecules and rotationally disordered H_2 molecules, can be described by the same cubic space group $Fd\bar{3}m$. With the origin choice 1, the O atoms sit in the $8a$ position $(0, 0, 0)$ and the center of mass of the H_2 molecules sit in either the $8b$ position $(1/2, 1/2, 1/2)$ for C_2 or the $16d$ position $(5/8, 5/8, 5/8)$ for C_3. Although the patterns of the C_2 and C_3 phases can be explained by the same space group, the two are easily distinguished due to the markedly different volume. This striking expansion of the water framework is due to the massive uptaking of H_2 molecules which double in number in C_3 with respect to the C_2 phase.

In the measurements before LH of the sample, our results point to the presence of the C_2 phase, persisting in a metastable state at all pressures. The obtained volumes for C_2 are in good agreement with the previous studies (13, 24, 33). Conversely, upon LH at about 40 GPa, we observe a clear change in the XRD pattern (Fig. 2 A and B) that corresponds to a volume increase of about 20% for hydrogen hydrate (Fig. 2C). The measured diffraction patterns, the equation of state, and the volume change are all in excellent agreement with the computational results for a transition from the C_2 to the C_3 phase. When C_3 forms at 40 GPa, its cubic unit cell has a volume of about 200 Å³ and contains 16 H_2 molecules. This corresponds to approx. 0.27 kg/L of H_2 (not including the hydrogen of the water). For reference, the H_2 weight % of the C_3 phase is 18.3. Once formed, C_3 remains stable up to the highest measured pressure.

Raman Spectroscopy Measurements and Related Computational Results. The results from the Raman measurements are summarized in Fig. 3, where we show selected spectra for the C_2 and C_3 phases as a function of pressure along different thermodynamic paths—with and without laser heating—along

with their simulated spectra, as well as the H_2 vibron frequencies versus pressure. As we will discuss in the following, the measured Raman spectrum becomes substantially different depending on whether LH is applied or not.

In Fig. 3, *Left*, we report the measured Raman spectra and frequencies as a function of pressure in two different sets of experiments in which LH was not applied. The Raman spectrum of the C_2 phase is characterized by a single peak (the peak at about 4,250 cm⁻¹ is due to the excess pure hydrogen in the sample), which becomes broader and whose frequency becomes higher as pressure increases. This peak is due to the vibron mode of the H_2 units in the structure. The observed extreme blueshift (mode hardening) with pressure is unlike in pure H_2, which exhibits a maximum frequency at approximately 38 GPa (34). The measured frequency for C_2, as well as its pressure dependence, is in excellent agreement with the previous literature (17, 23, 25, 33) and with our computed values. As shown in Fig. 3 A, *Left*, no other distinct peak appears, except for an extremely broad peak centered around 4,400 cm⁻¹, the frequency of which is substantially independent of pressure. This peak, which is hardly distinguishable from the background, probably stems from hydrogen being trapped in an amorphous form of hydrogen hydrate. In the samples on which we did not use LH, the C_2 phase persists up to the maximum investigated pressure of 90 GPa.

As shown in Fig. 3, *Right*, when LH is applied at 42 GPa, the Raman spectrum changes quite drastically: A total of three additional peaks appear at 4,480, 4,450, and 4,400 cm⁻¹. This observation is consistent with a transition from the C_2 to the C_3 phase, induced by the LH. The C_3 phase presents multiple peaks (see bottom spectrum of Fig. 3 B, *Right*) due to the presence of two symmetry-inequivalent H_2 molecules. In particular, while the centers of mass are equivalent, their lowest-energy orientations are not. Hence, on a qualitative level, the C_2 and C_3 phases can be distinguished by the occurrence of a series of satellite peaks in a range 200 cm⁻¹ below the main
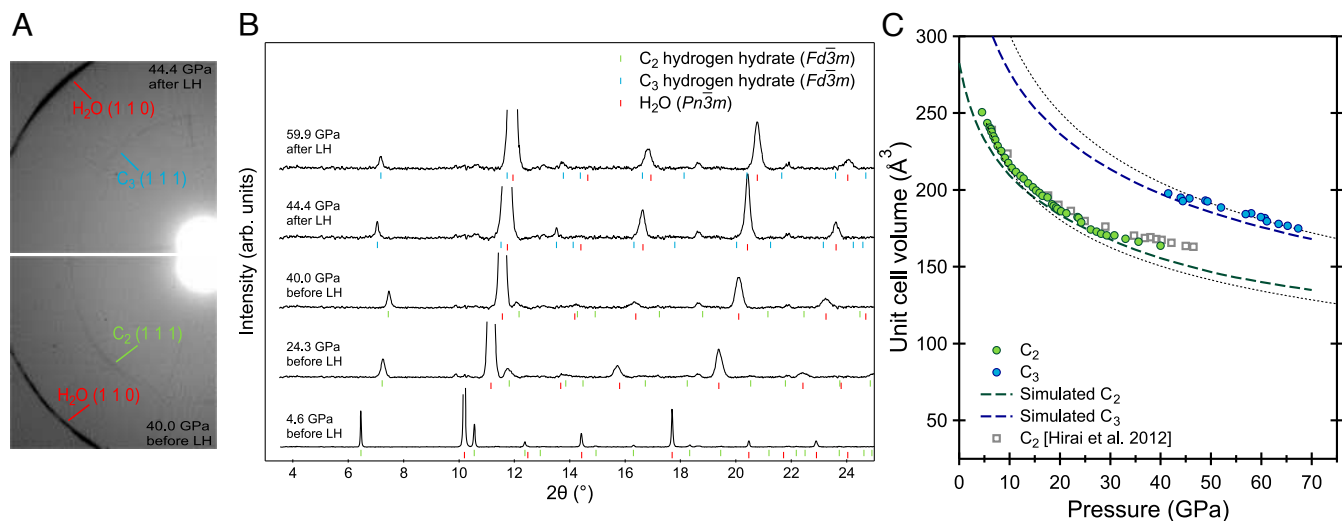

Fig. 2. XRD images (*A*) and patterns (*B*), and obtained volumes (*C*). (*A*) Details of two XRD images taken before and after laser heating, showing the first (and most intense) peak of hydrogen hydrate and of excess water ice. (*B*) Representative XRD patterns ($\lambda = 0.41$ Å) measured upon compression, before and after laser heating of the sample. The main (1 1 0) reflection of H_2O is not plotted entirely. The ticks correspond to the Bragg reflections of the refined structures: $(H_2O)H_2$ C_2 and $(H_2O)(H_2)_2$ C_3 hydrogen hydrate (both with space group $Fd\bar{3}m$), and H_2O ice VII (space group $Pn\bar{3}m$). The two weak peaks whose positions (18.65° and 21.9°) do not change with pressure are residual intensity from the masked diamond anvil peaks. (*C*) Unit cell volumes ($Z = 8$) as a function of pressure. Symbols represent experimental volumes and the values given in ref. 24 are reported as well. Dashed lines represent volumes derived from our DFT calculations and dotted lines represent the volumes of ideal mixtures of the equivalent amount of H_2O and H_2 molecules, calculated using the previously determined equations of state (31, 32).
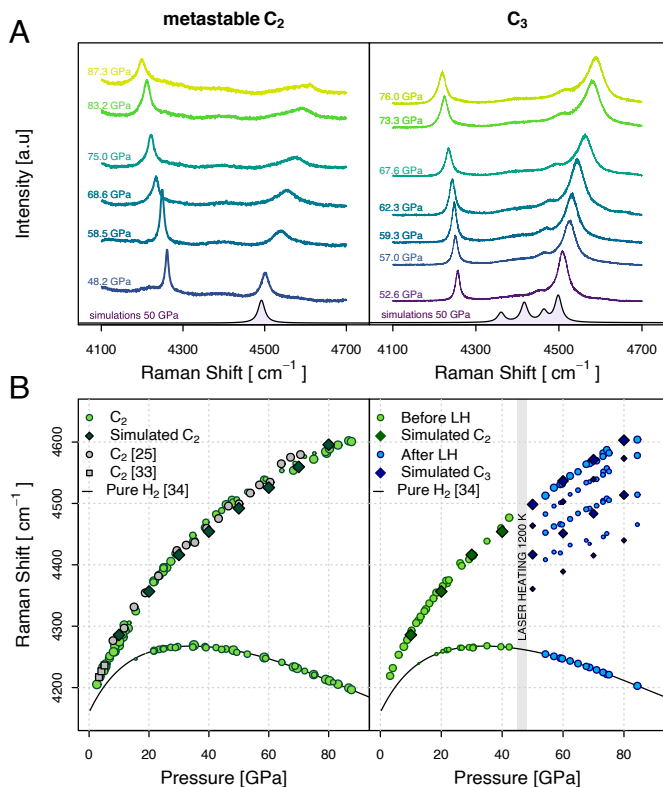
Fig. 3. Raman spectra (*A*) and vibron frequencies (*B*) for C_2 (*Left*) and C_3 (*Right*). (*A*) Representative experimental Raman spectra for the H_2 vibron at various pressures for the metastable C_2 (*Left*) and C_3 (*Right*) phases. Simulated Raman spectra at 50 GPa including an arbitrary frequency resolution are shown as black lines with filled areas for comparison. (*B*) Measured and calculated frequencies as a function of pressure for the C_2 (*Left*) and C_3 (*Right*) phase. The simulated frequencies account for both anharmonicity and DFT errors in the exchange-correlation functional as a uniform (pressure-independent) shift in frequency determined ab initio, whose details are reported in *SI Appendix*. The measured frequencies for the C_2 and C_3 phases are shown as green and blue dots, respectively. The calculated frequencies are shown as darker diamonds. Literature experimental data for the C_2 phase (25, 33) (gray symbols) and for pure solid H_2 (34) (black line) are also reported.

one. The computed phonon eigenvectors at the Γ point reveal how the differences in the environment of nonequivalent H_2 molecules (*SI Appendix*, Fig. S6) lead to substantially different energies in the H_2 vibron. The eight H_2 molecules in each primitive cell fall into two nonequivalent groups, based on their orientation with respect to the nearest oxygen atom. In particular, the observed peaks in order of increasing frequency correspond to the symmetric stretching of H_2 molecules pointing toward the nearest oxygen atom, the in- and out-of-phase stretching of all H_2 molecules, and the in- and out-of-phase stretching of H_2 molecules pointing orthogonally to the nearest oxygen atom, respectively. In simple terms, hydrogen atoms with their axis pointing toward the nearest oxygen atom exhibit a lower vibrational frequency than those pointing away from it, due to the induced perturbation from the excess negative charge around oxygen (*SI Appendix*, Fig. S6). Although these vibrational peaks become broader, they do remain visible up to the highest pressure measured.

Discussion

Summarizing the results of our XRD and Raman spectroscopy measurements, and the insight derived from our DFT and SSCHA calculations, we can finally reconcile all previous high-

pressure experiments within a single picture. From about 20 GPa, the C_2 phase starts to decompose into its components; this is because in the pressure range between approx. 20 and 30 GPa, the separated phases of pure water and hydrogen are more stable than both C_2 and C_3, as shown by our calculated enthalpy (*SI Appendix*, Fig. S4). This explains the appearance of the pure H_2 Raman vibron peak from about 20 GPa, which is also present in previous data (23). If the region of decomposition is avoided through fast compression (compression rate of ~5 GPa/s, as compared to a standard rate of typically 5 GPa/h), then no pure hydrogen is produced and we can follow the pressure shift of the C_2 Raman vibron peak without other contributions, as shown in *SI Appendix*, Fig. S7. As originally predicted in ref. 17, the C_3 phase is thermodynamically stable above approximately 30 GPa. However, at this pressure, the dense cubic ice framework prevents hydrogen diffusion, hence the C_2 phase can remain in a metastable state up to much higher pressures. This kinetic barrier can be overcome only by heating the sample and assuring hydrogen mobility, in the presence of a hydrogen basin. Indeed, we observe here that upon LH up to about 1,200 K, the system is able to overcome the barrier that separates it from the C_3 phase. Our computational results (*SI Appendix*, Figs. S8 and S9) also predict that upon compression of the C_2 phase above 20 GPa, the hydrogen molecules start to orient along the *c* axis, the hexagons of the water network elongate along the same direction, and the crystal symmetry is reduced from cubic to tetragonal, as observed in ref. 24. At even higher pressures, these local domains of symmetry-broken phases can favor amorphization due to the anisotropic compressibility of the C_2 phase, as observed in ref. 25. A similar guest orientational ordering was detected in the high-pressure phase III of methane hydrate (35, 36), before transition into a different structure at higher pressures.

We now discuss in further detail the structural properties of the high-pressure C_2 and C_3 phases. Despite sharing the same cubic ice skeleton for the water molecules, the C_2 and C_3 structures present a few key differences. These become clearer by considering the center of mass of the H_2 molecules (from here on named HCM), as shown in Fig. 4. In the C_2 phase, oxygens and HCMs form two identical diamond-like sublattices shifted by a $(1/2, 1/2, 0)$ vector (Fig. 4*C*). Indeed, at 40 GPa, the first O–O and H_2–H_2 distances are identical and equal to 2.35 Å (Fig. 4*A*). In the C_3 phase, however, the HCM network is markedly denser while the oxygen one expands; at the same pressure of 40 GPa, the nearest-neighbor H_2–H_2 distances are of about 2.0 Å, while the nearest neighbor O–O distances are of 2.5 Å (Fig. 4*B*): The oxygen sublattice has expanded to welcome further hydrogen molecules, which are thus closer packed. The HCMs form a network of corner-sharing tetrahedra (Fig. 4*D*) similar to those found in pyrochlores (37). Oxygen atoms sit at the center of a truncated tetrahedron (Fig. 4*E*), which consists of four hexagonal and four triangular faces. The vertexes of the truncated tetrahedron are occupied by HCMs, which implies that each oxygen is 12 coordinated with H_2 units. The hydrogen bond between water molecules, which ideally connects two oxygen atoms, passes through the center of one hexagon and is orthogonal to its plane (Fig. 4*E*). Intermolecular distances over a range of pressures up to 70 GPa are reported in *SI Appendix*, Fig. S9, where it is interesting to notice that the nearest-neighbor H_2-H_2 distances are very short in C_3 [shorter than in pure solid H_2 (32) at the same pressure].

To the best of our knowledge, the close-packed geometry of HCMs in the C_3 phase has never been observed in other filled
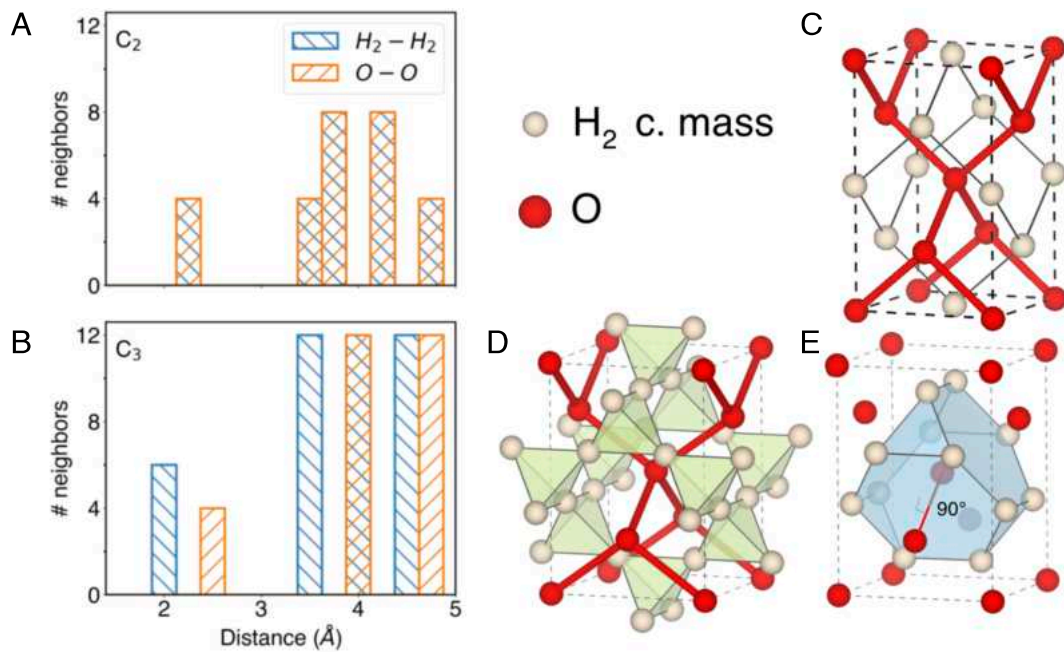
Fig. 4. Crystal structures of C_2 and C_3 highlighting the oxygen and H_2 sublattices. (*A* and *B*) Histograms of the number of neighboring O–O and H_2–H_2 as a function of distance in the C_2 and C_3 phase, respectively, at a pressure of 40 GPa. (*C*) Crystal structure of C_2. (*D* and *E*) Crystal structure of C_3. Oxygen atoms and H_2 centers of mass are shown as red and white spheres, respectively.

ice structures and account for the very high hydrogen density of this hydrate. While several gas hydrates were reported to have structural transitions at about 1–2 GPa (7, 8), hydrogen hydrate is only the second gas hydrate to show a phase transition above 10 GPa and to survive Megabar pressures. For methane hydrate, a structural transition from phase III (MH-III) to phase IV (MH-IV) is observed under compression to about 40 GPa at room temperature (36, 38). This is a transition between two different water sublattices for a constant methane-to-water molar ratio. Comparing the water frameworks, we can identify a common skeleton of all the filled ice structures showing remarkable high-pressure stability: the C_2 and C_3 phases and the methane hydrate phase MH-IV (36) share the ice I frame, either ice I*h* or ice I*c*, as shown in Fig. 5. The recurrence of the ice I network at high pressure is the result of an optimal compromise between the maximization of the hydrogen bond strength and a low efficiency-
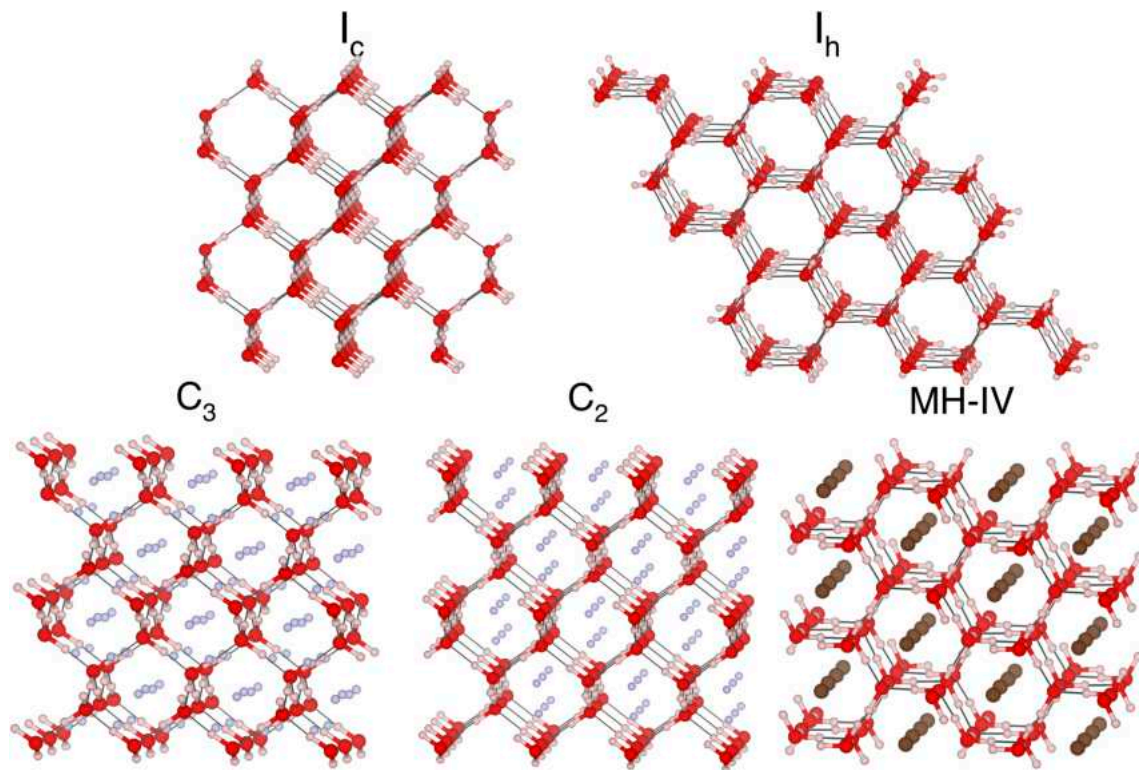

Fig. 5. Comparison between the crystal structures of the (low-pressure) water ice phases I*h* and I*c* and those of the related (high-pressure) phases C_2 and C_3 of hydrogen hydrate, and MH-IV of methane hydrate. Oxygen and hydrogen atoms of the water molecules are shown as large red and small pink spheres in a ball-and-stick model. The centers of mass of H_2 and CH_4 are shown as cyan and brown spheres, respectively. Hydrogen bonds are shown as black solid lines.

packed water structure—about 1/3 for both ice I*h* and I*c*—which thus retains the ability to host small molecules.

The high-pressure phase of methane hydrate (MH-IV) has been shown to survive to pressure up to 150 GPa at least (36); however, it is presently unclear whether it is thermodynamically stable or only metastable (see for example ref. 39). The volume of methane hydrate is indeed higher than that of the sum of its separated components (water ice and pure solid methane), in both phases MH-III and MH-IV. The comparison between the volume of methane hydrate (38) and of the components (31, 40) is reported in *SI Appendix,* Fig. S10. On the other hand, the hydrogen hydrate phase C_2 also has a larger volume than the sum of its separated pure components but C_3 is presently unique in being slightly denser than its constituent elements (Fig. 2*C*). According to our calculations, C_3 remains thermodynamically stable against decomposition up to 200 GPa at least (*SI Appendix,* Fig. S1). By contrast, the hydrates of argon, krypton, xenon, and carbon dioxide have all been reported to fully decompose upon compression to pressures of about 1 to 6 GPa (41, 42), and for nitrogen hydrate, a recent work reported no stable solid phases from 5 GPa to 140 GPa (43). Yet, it seems unlikely that methane and hydrogen hydrates are exceptions and future studies will be able to verify whether other small non-polar guests, such as for example, helium, neon, or dioxygen can form a similar structure with water at extreme pressures. It is possible that an entire class of filled ice I gas hydrates exists at pressures compatible with those encountered in the interior of large gaseous and icy planets of our solar system or Neptune-like exoplanets.

Materials and Methods

Experimental Details. Starting polycrystalline hydrogen hydrate samples having the clathrate sII structure were prepared by exposing H_2O ice (I*h*) to gas H_2 at 0.28 GPa for 20–30 min, following the method described in ref. 44. The ice was made of spheres with typical diameters of a few tens of micrometers. After preparation, the samples were recovered at ambient pressure and stored at liquid nitrogen temperature. For the high-pressure experiments, a small amount of sample was loaded at low temperature in a diamond anvil cell that was partially immersed in a liquid nitrogen bath. The loaded sample was then compressed to pressures of a few GPa before being warmed up to room temperature. This is a similar loading procedure to what we had previously done for methane hydrate (35, 36). This procedure inevitably produces a mixture of C_2 hydrogen hydrate and excess pure ice, because of the difference in molar ratios between the clathrate sII phase and the C_2 phase. Clathrate sII samples prepared following our method have a molar ratio $H_2O:H_2$ between 4 and 5, as we have verified by neutron diffraction in the past (44), and the C_2 phase is characterised by a molar ratio of 1. One sample was prepared directly in the DAC by loading room-temperature liquid H_2O and high-pressure H_2 at 0.14 GPa using a gas loading setup. This sample was measured by Raman spectroscopy and by XRD. Similarly to the cryo-loaded samples, it also formed hydrogen hydrate with the structure C_2 and after laser heating at 40 GPa, with the structure C_3. Some of the samples contained a small amount of pure N_2 and/or pure O_2, both of which can be easily identified from their respective vibron Raman peaks. Those must have been trapped in the sample chamber during cryo-loading and acted as a pressure-transmitting medium. Some of the samples did not contain N_2 or O_2 and an example of Raman spectrum for such a sample is reported in *SI Appendix,* Fig. S11. Culet diameters ranging between 100 and 300 μm for the diamond anvils were employed. Re-foil gaskets were used to contain the sample.

A Nd-YAG laser system (wavelength of 1.064 μm) was employed to heat the sample, using gold as the laser coupler. Angle-dispersive X-ray powder diffraction patterns were acquired at ID15b at ESRF (Grenoble, France) using a monochromatic X-ray beam ($λ = 0.41$ Å) and an Eiger 2 9M CdTe flat-panel detector, with a typical acquisition time of a few seconds. The beam spot size was 6×6 μm. The 2D diffraction patterns were treated to mask the Bragg

peaks of the diamond anvils then integrated into one-dimensional patterns, and a smooth polynomial background was subtracted. Le Bail refinements were performed using FullProf. In the XRD measurements, pressure was determined using the equation of state of gold from ref. 45. Raman spectra were acquired using a commercial Horiba Jobin–Yvon LabRam HR800 Raman spectrometer in a backscattering geometry, equipped with a COBOLT SambaTM 1000-mW green laser. Acquisition time was typically of about a minute. A smooth background was subtracted from the Raman spectra before fitting the data and examples of fits for C_2 and C_3 at 50 and 75 GPa are reported in *SI Appendix,* Fig. S12. Reference spectra were recorded at each pressure from the gasket close to the sample chamber and particular care was taken to check the effect of the background subtraction on the fit results. In the Raman measurements, pressure was determined by the shift of the R1 ruby fluorescence line (46), from the edge of the stressed diamond signal (47) or from the vibron frequency of pure solid H_2 (34). All measurements were performed at room temperature.

Many sample loadings were performed for this study, as mentioned above, and Fig. 3 results from data merged together from different loadings. In *SI Appendix,* Fig. S13, we show Raman spectra and corresponding vibron frequencies for one single sample loading over the whole investigated pressure range, before and after laser heating. Several loaded samples were compressed and measured by Raman spectroscopy without performing laser heating, applying different compression rates to check whether the C_3 phase would form. Some indications of the possible formation of a small amount of C_3 at room temperature above 70 GPa have been observed in some of the Raman experiments (*SI Appendix,* Fig. S14) but this point requests further investigation. One sample containing the C_2 phase was decompressed and measured by Raman spectroscopy. The corresponding frequencies are reported in panel *A* of *SI Appendix,* Fig. S15, where it can be seen that the pressure dependence of the peak frequencies is the same upon compression and decompression. Furthermore, we observe that no major changes occur upon decompression in the relative peak intensities of C_2 hydrogen hydrate and of pure H_2, meaning that the partial decomposition of the hydrate is irreversible. We also decompressed the C_3 phase by Raman spectroscopy and observed it can be recovered down to at least 36 GPa at room temperature (*SI Appendix,* Fig. S15*B*). The stability of the C_3 phase under decompression is an important information in order to envisage the use of high-density hydrates as H_2 storage material and future studies will be able to check whether the C_3 phase can be recovered at ambient pressure and low temperature.

Simulation Methods. Crystal structure prediction was performed using evolutionary algorithm as implemented in the USPEX code (27, 28). The structures were relaxed using a five-step process with the Vienna ab initio simulation package (VASP) as a DFT code (48), employing the projector-augmented wave pseudopotentials with Perdew–Burke–Ernzerhof pseudopotentials provided with the package (49). Further details are provided in *SI Appendix*.

The C_2 and C_3 phases were simulated using Density Functional (Perturbation) Theory as implemented in Quantum ESPRESSO (50, 51), using Optimized Norm-Conserving Vanderbilt pseudopotentials (ONCV) (52) and optimized Becke88 van der Waals exchange-correlation functional (53–55). A cutoff of 90 Ry was employed on the plane waves' expansion, and the integration of the Brillouin zone was performed over a $4×4×4$ grid in reciprocal space with fixed occupations. The vibrational zero-point energy was computed within the harmonic approximation over a $2×2×2$ grid in reciprocal space, and integrated over a $8×8×8$ grid using Fourier interpolation. We did not include temperature effects in our calculations of the thermodynamics properties. Proton-ordered configurations for the water molecules satisfying the Bernal–Fowler rules were obtained directly from the USPEX structural search calculations. Furthermore, consideration of the H_2 molecules as two individual atoms lowers the crystal symmetry in the simulations: The simulated structures are not cubic but tetragonal or orthorhombic (see *SI Appendix* for further details). Details of our C_2 and C_3 structures and unit cell dimensions as a function of pressure, calculated within DFT, are reported in *SI Appendix,* Table S2 and Fig. S8, respectively. For pure hydrogen and pure water, we used as references the (proton-ordered) structures of phase II (56) and ice VIII, respectively.

Anharmonicity and quantum nuclear effects were evaluated using the stochastic self-consistent harmonic approximation as implemented in the SSCHA

code (29, 30). The SSCHA minimizes the free energy $F[\hat{\rho}] = \langle H \rangle_{\hat{\rho}} - TS[\hat{\rho}]$ by optimizing a trial density matrix $\hat{\rho}$ constrained among solutions of an auxiliary harmonic Hamiltonian. The free energy minimization is performed using the second-order Newton method, with a stochastic sampling of the Born–Oppenheimer energy landscape at DFT level (30). The method allowed us to evaluate the strength of quantum and anharmonic effects in the frequencies of the hydrogen vibron compared to the harmonic approximation. This method has been reported as the most successful to compute the phase diagram and Raman and IR spectra of H_2 vibrons at high pressure (57–60). The interested reader can find further information on the specific details employed in the simulation of C_2 and C_3 in *SI Appendix* and additional details on the numerical implementation in ref. 29.

Data, Materials, and Software Availability. All study data are included in the article and/or *SI Appendix*.

Author affiliations: [a]Dipartimento di Fisica, Sapienza Università di Roma, 00185 Roma, Italy; [b]Centre for Science at Extreme Conditions and School of Physics and Astronomy, University of Edinburgh, EH9 3FD Edinburgh, United Kingdom; [c]Institut für Festkörperphysik, Technische Universität Wien, 1040 Wien, Austria; [d]Laboratory of Quantum Magnetism, Institute of Physics, École Polytechnique Fédérale de Lausanne, CH-1015 Lausanne, Switzerland; [e]Theory and Simulation of Materials, and National Centre for Computational Design and Discovery of Novel Materials, École Polytechnique Fédérale de Lausanne, 1015 Lausanne, Switzerland; [f]Consiglio Nazionale delle Ricerche, Istituto Nazionale di Ottica, CNR-INO, Sesto Fiorentino, 50019, Italy; [g]European Laboratory for Nonlinear Spectroscopy, LENS, Sesto Fiorentino (FI), 50019, Italy; and [h]Sorbonne Université, UMR CNRS 7590, Institut de Minéralogie, de Physique des Matériaux et de Cosmochimie, 75252 Paris, France

1. J. H. Waite *et al.*, Cassini finds molecular hydrogen in the Enceladus plume: Evidence for hydrothermal processes. *Science* **356**, 155–159 (2017).
2. A. Bouquet, O. Mousis, J. H. Waite, S. Picaud, Possible evidence for a methane source in Enceladus' ocean. *Geophys. Res. Lett.* **42**, 1334–1339 (2015).
3. A. Bouquet, O. Mousis, C. R. Glein, G. Danger, J. H. Waite, The role of clathrate formation in Europa's ocean composition. *Astrophys. J.* **885**, 14 (2019).
4. E. S. Kite, E. B. Ford, Habitability of exoplanet waterworlds. *Astrophys. J.* **864**, 75 (2018).
5. W. L. Mao *et al.*, Hydrogen clusters in clathrate hydrate. *Science* **297**, 2247–2249 (2002).
6. E. Sloan, C. Koh, *Clathrate Hydrates of Natural Gases* (CRC Press, ed. 3, 2008).
7. J. Loveday, E. Nelmes, High pressure hydrates. *J. Phys. Chem. Chem. Phys.* **10**, 937–950 (2008).
8. L. E. Bove, U. Ranieri, Salt- and gas-filled ices under planetary conditions. *Philos. Trans. R. Soc. A* **377**, 20180262 (2019).
9. M. E. Donnelly, P. Teeratchanan, C. L. Bull, A. Hermann, J. S. Loveday, Ostwald's rule of stages and metastable transitions in the hydrogen-water system at high pressure. *Phys. Chem. Chem. Phys.* **20**, 26853–26858 (2018).
10. D. M. Amos *et al.*, A chiral gas-hydrate structure common to the carbon dioxide-water and hydrogen-water systems. *J. Phys. Chem. Lett.* **8**, 4295–4299 (2017).
11. L. del Rosso, M. Celli, L. Ulivi, New porous water ice metastable at atmospheric pressure obtained by emptying a hydrogen-filled ice. *Nat. Commun.* **7**, 13394 (2016).
12. T. A. Strobel, M. Somayazulu, S. V. Sinogeikin, P. Dera, R. J. Hemley, Hydrogen-stuffed, quartz-like water ice. *J. Am. Chem. Soc.* **138**, 13786–13789 (2016).
13. W. L. Vos, L. W. Finger, R. J. Hemley, H. Kwang Mao, Novel H_2–H_2O clathrates at high pressures. *Phys. Rev. Lett.* **71**, 3150–3153 (1993).
14. Y. Wang *et al.*, Novel hydrogen clathrate hydrate. *Phys. Rev. Lett.* **125**, 255702 (2020).
15. C. G. Salzmann, Advances in the experimental exploration of water's phase diagram. *J. Chem. Phys.* **150**, 060901 (2019).
16. K. Komatsu, Neutrons meet ice polymorphs. *Crystallogr. Rev.* **28**, 224–297 (2022).
17. G. R. Qian, A. O. Lyakhov, Q. Zhu, A. R. Oganov, X. Dong, Novel hydrogen hydrate structures under pressure. *Sci. Rep.* **4**, 5606 (2014).
18. L. Hakim, K. Koga, H. Tanaka, Phase behavior of different forms of ice filled with hydrogen molecules. *Phys. Rev. Lett.* **104**, 115701 (2010).
19. J. Zhang, J. L. Kuo, T. Iitaka, First principles molecular dynamics study of filled ice hydrogen hydrate. *J. Chem. Phys.* **137**, 084505 (2012).
20. G. S. Smirnov, V. V. Stegailov, Toward determination of the new hydrogen hydrate clathrate structures. *J. Phys. Chem. Lett.* **4**, 3560–3564 (2013).
21. J. Košata, P. Merkl, P. Teeratchanan, A. Hermann, Stability of hydrogen hydrates from second-order Møller–Plesset perturbation theory. *J. Phys. Chem. Lett.* **9**, 5624–5629 (2018).
22. T. Ikeda, Simulating Raman spectra of hydrogen hydrates using first-principles path-integral ring-polymer molecular dynamics. *Chem. Phys. Lett.* **792**, 139416 (2022).
23. S. Machida, H. Hirai, T. Kawamura, Y. Yamamoto, T. Yagi, Raman spectra for hydrogen hydrate under high pressure: Intermolecular interactions in filled ice Ic structure. *J. Phys. Chem. Solids* **71**, 1324–1328 (2010).
24. H. Hirai *et al.*, Structural changes of filled ice Ic hydrogen hydrate under low temperatures and high pressures from 5 to 50 GPa. *J. Chem. Phys.* **137**, 074505 (2012).
25. S. I. Machida, H. Hirai, T. Kawamura, Y. Yamamoto, Y. Yagi, Isotopic effect and amorphization of deuterated hydrogen hydrate under high pressure. *Phys. Rev. B* **83**, 144101 (2011).
26. W. L. Mao, H. Kwang Mao, Hydrogen storage in molecular compounds. *Proc. Natl. Acad. Sci. U.S.A.* **101**, 708–710 (2004).
27. C. W. Glass, A. R. Oganov, N. Hansen, USPEX-evolutionary crystal structure prediction. *Comput. Phys. Commun.* **175**, 713–720 (2006).
28. A. O. Lyakhov, A. R. Oganov, H. T. Stokes, Q. Zhu, New developments in evolutionary structure prediction algorithm USPEX. *Comput. Phys. Commun.* **184**, 1172–1182 (2013).
29. L. Monacelli *et al.*, The stochastic self-consistent harmonic approximation: Calculating vibrational properties of materials with full quantum and anharmonic effects. *J. Phys.: Condens. Matter* **33**, 363001 (2021).
30. L. Monacelli, I. Errea, M. Calandra, F. Mauri, Pressure and stress tensor of complex anharmonic crystals within the stochastic self-consistent harmonic approximation. *Phys. Rev. B* **98**, 024106 (2018).
31. S. Klotz *et al.*, Bulk moduli and equations of state of ice VII and ice VIII. *Phys. Rev. B* **95**, 174111 (2017).
32. P. Loubeyre *et al.*, X-ray diffraction and equation of state of hydrogen at megabar pressures. *Nature* **383**, 702–704 (1996).
33. T. A. Strobel, M. Somayazulu, R. J. Hemley, Phase behavior of H_2 + H_2O at high pressures and low temperatures *J. Phys. Chem. C* **115**, 4898–4903 (2011).
34. R. T. Howie, C. L. Guillaume, T. Scheler, A. F. Goncharov, E. Gregoryanz, Mixed molecular and atomic phase of dense hydrogen. *Phys. Rev. Lett.* **108**, 125501 (2012).
35. S. Schaack *et al.*, Orientational ordering, locking-in, and distortion of CH_4 molecules in methane hydrate III under high pressure. *J. Phys. Chem. C* **122**, 11159–11166 (2018).
36. S. Schaack *et al.*, Observation of methane filled hexagonal ice stable up to 150 GPa. *Proc. Natl. Acad. Sci. U.S.A.* **116**, 16204–16209 (2019).
37. J. S. Gardner, M. J. P. Gingras, J. E. Greedan, Magnetic pyrochlore oxides. *Rev. Mod. Phys.* **82**, 53 (2010).
38. H. Kadobayashi *et al.*, Structural evolution of methane hydrate under pressures up to 134 GPa. *J. Chem. Phys.* **152**, 194308 (2020).
39. N. Pantha, N. P. Adikhari, S. Scandolo, Decomposition of methane hydrates at high pressure: A density-functional theory study. *High Press. Res.* **35**, 231–238 (2015).
40. L. Sun *et al.*, X-ray diffraction studies and equation of state of methane at 202 GPa. *Chem. Phys. Lett.* **473**, 72–74 (2009).
41. H. Hirai, T. Tanaka, T. Kawamura, Y. Yamamoto, T. Yagi, Structural changes in gas hydrates and existence of filled ice structure of methane hydrate above 40 GPa. *J. Phys. Chem. Solids* **65**, 1555–1559 (2004).
42. H. Hirai *et al.*, Phase changes of CO_2 hydrate under high pressure and low temperature. *J. Chem. Phys.* **133**, 124511 (2010).
43. X. Zhang *et al.*, Immiscibility in N_2–H_2O solids up to 140 GPa. *J. Chem. Phys.* **154**, 234505 (2021).
44. U. Ranieri *et al.*, Quantum dynamics of H_2 and D_2 confined in hydrate structures as a function of pressure and temperature. *J. Phys. Chem. C* **123**, 1888–1903 (2019).
45. Y. Fei *et al.*, Toward an internally consistent pressure scale. *Proc. Natl. Acad. Sci. U.S.A.* **104**, 9182–9186 (2007).
46. G. Shen *et al.*, Toward an international practical pressure scale: A proposal for an IPPS ruby gauge (IPPS-Ruby2020). *High Pres. Res.* **40**, 299–314 (2020).
47. Y. Akahama, H. Kawamura, Pressure calibration of diamond anvil Raman gauge to 310 GPa. *J. Appl. Phys.* **100**, 043516 (2006).
48. G. Kresse, J. Furthmüller, Efficient iterative schemes for ab initio total-energy calculations using a plane-wave basis set. *Phys. Rev. B* **54**, 11169–11186 (1996).
49. G. Kresse, D. Joubert, From ultrasoft pseudopotentials to the projector augmented-wave method. *Phys. Rev. B* **59**, 1758–1775 (1999).
50. P. Giannozzi *et al.*, QUANTUM ESPRESSO: A modular and open-source software project for quantum simulation of materials. *J. Phys.: Condens. Matter* **21**, 395502 (2009).
51. P. Giannozzi *et al.*, Advanced capabilities for materials modelling with quantum espresso. *J. Phys.: Condens. Matter* **29**, 465901 (2017).
52. D. R. Hamann, Optimized norm-conserving Vanderbilt pseudopotentials. *Phys. Rev. B* **88**, 085117 (2017).
53. G. Graziano, J. Klimeš, F. Fernandez-Alonso, A. Michaelides, Improved description of soft layered materials with van der Waals density functional theory. *J. Phys.: Condens. Matter* **24**, 424216 (2012).
54. T. Thonhauser *et al.*, Van der Waals density functional: Self-consistent potential and the nature of the van der Waals bond. *Phys. Rev. B* **76**, 125112 (2007).
55. R. Sabatini, E. Küçükbenli, B. Kolb, T. Thonhauser, S. de Gironcoli, Structural evolution of amino acid crystals under stress from a non-empirical density functional. *J. Phys.: Condens. Matter* **24**, 424209 (2012).

56. C. Pickard, R. Needs, Structure of phase III of solid hydrogen. *Nat. Phys.* **3**, 473–476 (2007).
57. L. Monacelli, I. Errea, M. Calandra, F. Mauri, Black metal hydrogen above 360 GPa driven by proton quantum fluctuations. *Nat. Phys.* **17**, 63–67 (2020).
58. L. Monacelli, M. Casula, K. Nakano, S. Sorella, F. Mauri, Quantum phase diagram of high-pressure hydrogen. *Nat. Phys.* **19**, 845–850 (2023).
59. L. Monacelli, F. Mauri, Time-dependent self-consistent harmonic approximation: Anharmonic nuclear quantum dynamics and time correlation functions. *Phys. Rev. B* **103**, 104305 (2021).
60. A. Siciliano, L. Monacelli, G. Caldarelli, F. Mauri, Wigner Gaussian dynamics: Simulating the anharmonic and quantum ionic motion. *Phys. Rev. B* **107**, 174307 (2023).